Supplementary Materials for

Dendritic action potentials and computation in human layer 2/3 cortical neurons

Albert Gidon, Timothy Adam Zolnik, Pawel Fidzinski, Felix Bolduan, Athanasia Papoutsi, Panayiota Poirazi, Martin Holtkamp, Imre Vida, Matthew Evan Larkum*

*Corresponding author. Email: matthew.larkum@hu-berlin.de

Published 3 January 2020, *Science* **367**, 83 (2020)
DOI: 10.1126/science.aax6239

This PDF file includes:

Materials and Methods

Human tissue transport and preparation

All human experiments were approved by the Ethics Committee of the Charité – Universitätsmedizin Berlin and performed in agreement with the Declaration of Helsinki. Neocortical tissue used in this study was obtained from resections of the anterior temporal lobe of twenty-seven epilepsy patients and of three brain tumor patients (**Table S1**). All patients had given written consent prior to the procedure. The brain tissue used in this study was presumably non-pathological, as it was not located in the area of the seizure focus or the tumor. Immediately after removal, tissue was transferred to carbonated (95% O2, 5% CO2), ice-cold transport protective solution; either "NMDG" [containing (in mM) NMDG (93), HCl (93), KCl (2.5), NaH2PO4 (1.2), NaHCO3 (30), MgSO4 (10), CaCl2 141 (0.5), HEPES (20), glucose (25), Na-L-ascorbate (5), thiourea (2), Na-pyruvate (3) (ref *3*)] or in "Choline" solution [containing (in mM) Choline chloride (110), KCl (2.5), NaH2PO4 143 (1.25), NaHCO3 (26), MgCl2 (7), CaCl2 (0.5), glucose (10), Na-L-ascorbate (11.6), Na-144 pyruvate (3.1) (ref *37*)] and transported within 10-40 minutes to the location where pia was carefully removed and then transported a second time, within 5 minutes in the same ice-cold transport solution, to the laboratory for slicing and recording. Tissue resected from tumor patients was transported and sliced in "Sucrose" solution [containing (in mM) NaCl (87), NaH2PO4 (1.25), KCl (2.5), CaCl2 (0.5), MgCl2 (3) Glucose (10), NaHCO3 (25), Saccharose (75)]. Cortical tissue was sliced to thickness of 300-350 µm with Leica 1200vt vibrotome in protective Choline solution with the blade oriented as orthogonally to the pia as possible to maintain complete dendrites. Slices were incubated in either "HEPES" solution [identical to NMDG solution but with NaCl (92) instead of NMDG (93) and HCl (93)

(ref *38*)] or "aCSF" [containing (in mM) NaCl (125), KCl (2.5), NaH2PO4 (1.25), NaHCO3 (25), MgCl2 (1), CaCl2 141 (1), glucose (25)] solution in 35° C for at least 30 minutes and then stored in aCSF continuously perfused with carbogen for the rest of the experiment in room temperature no longer than 24 hours.

Electrophysiology

Slices were submerged in the recording chamber and perfused with aCSF (~2 ml/min) and heated to 33-35°C (Scientifica). Single L2/3 pyramidal neurons were identified using infrared Dodt gradient contrast and a CCD camera (CoolSnap ES2; Roper Scientific). Data were acquired with InstruTECH ITC-18 board and custom software written in Igor (Igor 6.22A; Wavemetrics). The direct (point-to-point) distance of the soma from pia and the distance of the dendritic electrode from the soma were measured during the recording session. Cells were chosen randomly. Recording pipettes were filled with intracellular solution containing 0.1% Biocytin and (in mM), K-gluconate (130), KCl (20), Mg-ATP (4), Na_2-phosphocreatine (10), GTP-Tris (0.3), HEPES (10). The pH was adjusted with KOH to 7.25 – 7.30. Osmolality was 300 mosmol l^{-1}. In addition, the somatic pipette contained 10 – 20 μM Alexa 594 (Invitrogen).

Dual whole-cell voltage recordings were performed from the soma and dendrites using Dagan BVC-700A amplifiers (Dagan Minneapolis, USA) with low pass filter set to 5 KHz. We did not correct for liquid junction potential. Pipette resistance and access resistance were typically 4 – 12 MΩ and 12 – 20 MΩ for the somatic pipette. Due to the small diameter (*3*) of the dendrites of L2/3 neurons, the dendritic pipette resistance and access resistance was 14 – 32 MΩ and 40 – 200 MΩ respectively (*39*).

Access resistance and capacitance were continuously monitored for the dendritic electrode in current clamp mode. For the voltage attenuation plot in **Fig. S1**D, in addition to the manual compensation of the dendritic pipette access resistance during the experiment, we further corrected access resistance offline by fitting single exponential curve to the last 4 ms of the voltage response to the current test pulse (test pulse had duration of 5 ms and amplitude of –60 nA). Then, the exponential fit was extrapolated to the beginning of the stimulus time to get the expected voltage. The difference between the experimentally measured voltage and the voltage computed by the exponential fit was used to find the additional access resistance which was insufficiently compensated during the experiment.

Statistical analysis

Wilcoxon rank-sum test for two independent samples was used using Igor (WaveMetrix) built-in operation.

Visualization of biocytin-filled neurons

To morphologically identify and characterize recorded neurons, the acute human slices were processed for histology as previously described (*40*). In brief, slices were fixed at least for 24 hours in phosphate buffered (PB) solution (0.1 M) containing 4% paraformaldehyde. Subsequently, slices were intensely rinsed and incubated with Alexa Flour 647-conjugated streptavidin (Invitrogen, UK, dilution 1:1000 in PB, including 0.1% Triton-X100 as detergent) overnight at 4°C. Slices were finally mounted in an aqueous mounting medium (Fluoromount, Southern Biotech, AL, USA) either on glass slides with a cover slip or between two coverslips with a 300 µm metal spacer.

Confocal imaging and reconstruction of neurons

Cells were imaged on a laser scanning confocal microscope (FluoView 1000, Olympus) using a 20x (N.A 0.75) or a 30x (N.A 1.05) silicon oil-immersion objective. Image stacks were collected at 1024x1024 resolution in the horizontal plan (2µs pixel dwell time) and 1 µm steps along the Z-axis. Image stacks covering the full extent of the neuron were stitched using the FIJI software package (*41*) (http://fiji.sc) and 3D reconstructions of the somato-dendritic domain of selected cells were performed using the neuTube software package (*42*).

Two–photon imaging.

Cells were filled with 100 µM Oregon-green 488 BAPTA-1 (Thermo Fischer, Wlatham, MA) by dialysis from the patch pipette in whole-cell configuration. Cells were stimulated 10x with 2 ms current steps at 50 Hz and 200 Hz. Line scan recordings began typically 40 minutes (~ 30–120 min) after break-in and were performed chronologically from soma to dendrite. Data acquisition was performed using MATLAB (MathWorks Inc.) based MES software package (Femtonics). Calcium signals were imaged with a Femto 2D two-photon laser scanning system (Femtonics Ltd, Budapest, Hungary) equipped with a femtosecond pulsed Chameleon Ti:Sapphire laser (Coherent, Santa Clara, CA, USA) tuned to $\lambda = 800$ nm. Fluorescence was detected in epifluorescence mode with a water immersion objective (LUMPLFL ×60/1.0 NA, Olympus, Hamburg, Germany) and 525/50 bandpass filter. Trans-fluorescence and transmitted infrared light were detected using an oil immersion condenser (Olympus; 1.4 NA).

Fluorescence resulted from Ca^{2+} transients were acquired with 64-pixel line scans with an average 0.5 kHz sampling rate (minimum 48 Hz and maximum of 1.5 kHz). Individual traces

were oversampled offline (interpolation) to 1.5 kHz (i.e. maximum sample rate) and averaged over at least 4 repetitions and smoothed by 5 points boxcar filter. Ca^{2+} transients are reported here as the peak change in OGB-1 fluorescence ($F(t)$) normalized to the resting OGB fluorescence (F_0) after subtracting the background fluorescence from neighboring regions F_{bg},

$$\Delta F/F_0 = (F(t) - F_0)/(F_0 - F_{bg}). \quad (1)$$

The fluorescence against the distance from the soma were fitted by a skewed Gaussian curve using the equation $y = a(x-c)^b \times exp((x-c)^2/d^2)$ where *a*, *b*, *c*, and *d* are fitting parameters.

Computational model

We used a reconstruction of L2/3 neuron morphology (**Fig. 3A**), consisting of a somatic compartment, 101 basal dendritic sections, 81 apical tree sections and an axonal cable (1000 µm length, 1µm diameter). For each section compartment lengths were at most 30 µm. Membrane capacitance (C_m) and axial resistance (R_i) were uniformly set to 0.45 µF cm^2 (*43*) and 100 Ω×cm, respectively, over the entire dendrite. These values resulted in somatic input resistance (R_{in}) and membrane time constant (τ_m) of 39 MΩ and 17 ms, respectively, similar to the experimental values (R_{in} = 41 MΩ and τ_m = 14 ms). The soma was modeled with sodium (I_{Na}), potassium delayed rectifier (I_{Kdr}) currents, with the corresponding maximal conductances, g_{Na} = 0.1 S/cm^2 , g_K = 0.045 S/cm^2 and reversal potentials, E_K = –80 mV, E_{Na} = 90 mV. R_m was 37 MΩ×cm^2 in all compartments. The rate functions for the sodium and potassium channels where taken from (*44*), but all activation curves were shifted by –50 mV [originally –60 mV in (*45*)] to account for

somatic threshold we observed in the experiment (complete model for **Fig. 3** and **Fig. S9** is publically available in ModelDB)

dCaAPs were simulated at one dendritic compartment where threshold, width and amplitude as a function of the input strength were simulated by sum of current sources with a sigmoidal shape. Specifically, the dCaAP current,

$$I_{dCaAP} = -wK(v)(A - B), \quad (2)$$

was triggered when membrane potential crossed –36 mV where w was 1.6 and 4 such that the dCaAP amplitude was about 50 mV and 60 mV at threshold in **Fig. 3** and in **Fig. S9**, respectively.

A and B, the rise and decay of the dCaAP current were given by sigmoid functions $A = 1/(1 + exp(-(t - t')/\tau_A))$ and $B = 1/(1 + exp(-(t - (t' + \Delta t')/\tau_B))$ where t' is the dCaAP onset, $\Delta t'$ = 21 ms, τ_A = 3 ms and τ_B = 0.4 ms. The dendrite activation function, $K(v)$, which depended on membrane potential, [where in our passive dendritic model approximate dCaAP suppression as a function of the current $K(i)$], was

$$K(v) = exp[\frac{-F \times (v - v_{th})}{\tau_K}] \quad (3)$$

where v is the membrane potential at the location of the dCaAP, v_{th} is the threshold (–36 mV) for dCaAP, $F = 1/(v_{th} - v_{rest})$, is a normalization factor and τ_K, the dCaAP amplitude decay constant was 0.3 (dimensionless). The refractory period was explicitly set to 200 ms such that dCaAPs fired with 5 Hz or less. Synaptic model was done similarly to refs (*33*, *45*, *46*).

All the synapses were activated at 20 Hz in all the models. The synaptic current was modeled as, $I_{syn}(t,V) = g_{syn}(t,V) \times (V - E_{syn})$, where $g_{syn}(t,V)$ is the synaptic conductance change, and E_{syn} is the reversal potential for the synaptic current which was 0 mV for excitatory synapses and –75 mV for inhibitory synapses. The conductance change for AMPA, NMDA and GABA was modeled as

$$g_{syn}(t,V) = g_{max} \times N \times G \times (e^{-t/\tau_2} - e^{-t/\tau_1}), \quad (4)$$

where N is normalization factor such that g_{max} the peak conductance. g_{max} and time constants where as follows: $g_{max,AMPA}$ = 0.7 nS, $g_{max,NMDA}$ = 1.3 nS, $g_{max,GABA}$ =0.5 nS, $\tau_{1,AMPA}$ = 0.3 ms, $\tau_{2,AMPA}$ = 1.8 ms, $\tau_{1,NMDA}$ = 8 ms, $\tau_{2,NMDA}$ = 35 ms, $\tau_{1,GABA}$ = 2 and $\tau_{2,GABA}$ = 23 ms (**Fig. 3** and distal inhibition in **Fig. S9**), $\tau_{1,GABA\text{-}proximal}$ = 0.5 and $\tau_{2,GABA\text{-}proximal}$ = 5 ms (**Fig. S9**, proximal inhibition). For AMPA and GABA, we used G = 1, whereas for NMDA

$$G = \frac{1}{1 + e^{-\gamma v} \times [Mg^{2+}]/3.57}, \quad (5)$$

where [Mg^{2+}] is extracellular magnesium concentration of 1 mM, γ = 0.077 1/mV (*33*).

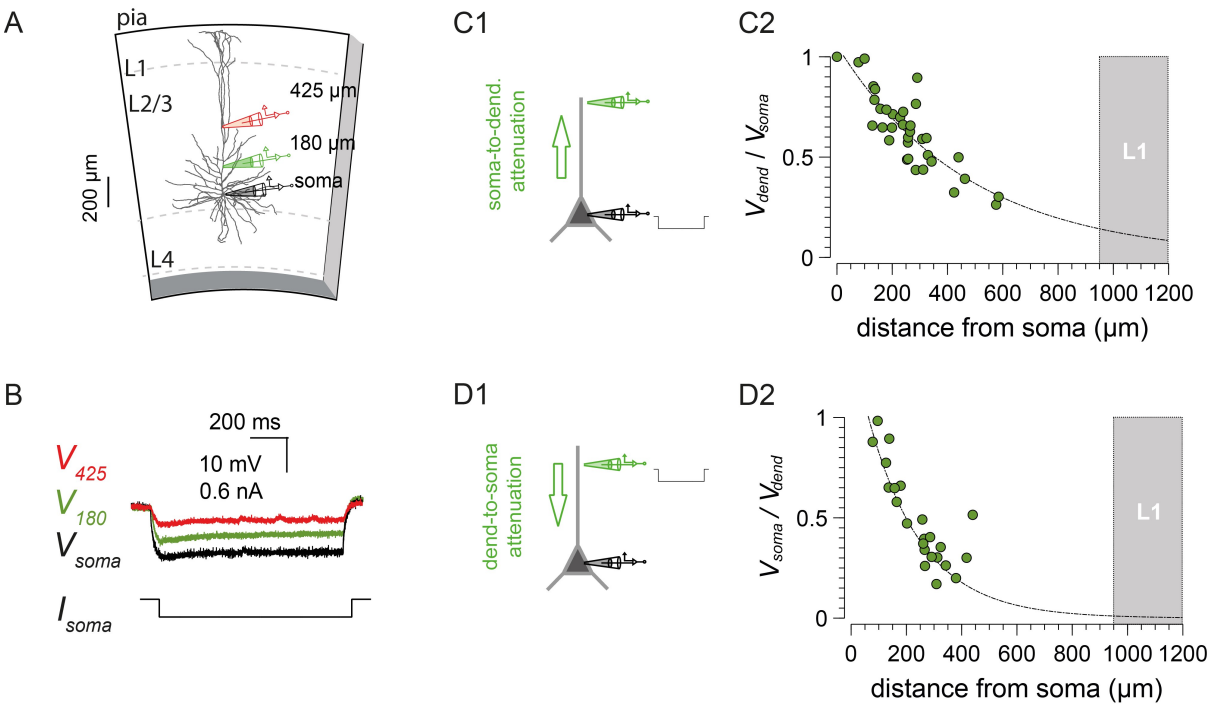

Fig. S1. Steady potentials are severely attenuated at the apical dendrite of layer 2/3 pyramidal neurons in the human cortex.

A. Reconstructed cortical layer 2/3 pyramidal neuron at a depth of 1098 µm from the pia. **B**. Two consequent dual recordings of soma and dendrites during somatic negative step current injection. The traces' color corresponds to the color of the patch clamp electrodes in **A** in the two dendritic sites. **C1**. Experimental schematic depicts stimulation (negative current step for one second) and recording site at the soma (black pipette) and a second recording site at the dendrite. **C2**. Attenuation of steady potentials (averaged for voltage traces between 800 and 1000 ms after stimulation onset; n = 34) from the soma to the dendrite (dendritic potential normalized by the somatic potential) plotted against the distance of the dendritic recording electrode. Length constant is λ = 475 µm (single exponential fit). Gray region on the graph depicts a putative region of layer 1 for the longest dendrites. **D1**. As in C1 but current was injected into the dendrite rather than the soma. **D2**. As in C2 but for the potential attenuation from the dendrite to the

soma. Length constant was λ = 195 µm (single exponential fit; n = 23; average R_{access} of 71.3 ± 19.5 MΩ ranging between 38.0 and 113.4 ms). The amplitude of the exponential fit in C2 and D2 was not constrained to value of 1 at the soma.

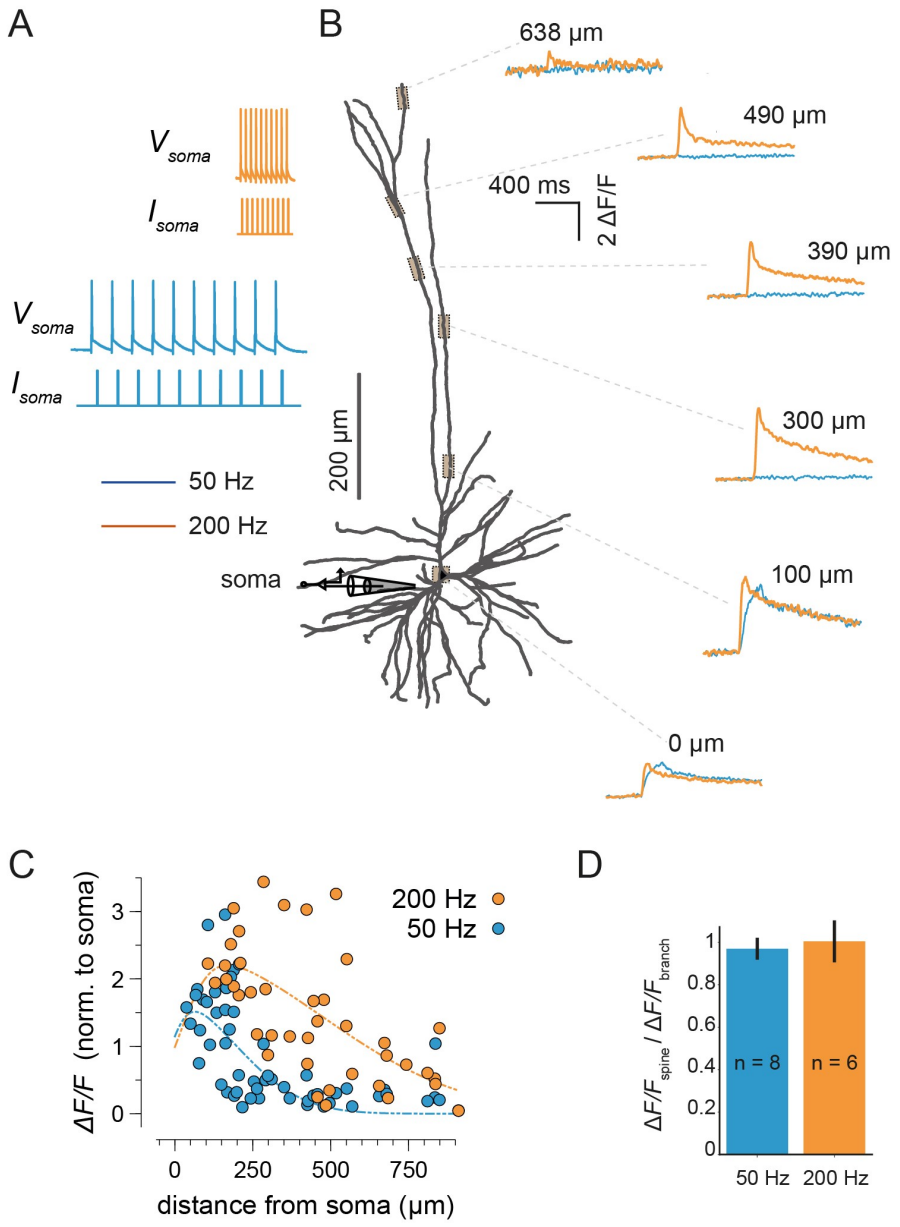

Fig. S2. 2-photon imaging indicates that APs invade the distal dendrite at high frequency.

A. AP bursts were evoked by injecting 10 supra-threshold current pulses of 2 ms duration at 50 Hz (blue traces) and at 200 Hz (orange traces) at the soma of layer 2/3 pyramidal neurons. **B.** Example of Ca^{2+} signals in a pyramidal neuron located 640 µm below the pia surface. Dendritic locations where imaged sequentially. $\Delta F/F$ traces are shown with corresponding color (blue and

orange for somatic pulses at 50 Hz and 200 Hz, respectively). **C.** Summary for amplitude of $\Delta F/F$ for somatic current pulse stimulation at 50 Hz (blue dots; n = 18 cells) and at 200 Hz (orange dots; n = 13 cells). Note the enhanced $\Delta F/F$ response for stimulation at 200 Hz [fitted with scaled skewed Gaussian (*4*)]. **D**. Ca^{2+} signal at the spine ($\Delta F/F_{spine}$) was very similar to the corresponding signal at the branch ($\Delta F/F_{branch}$) for both 50 Hz and 200 Hz APs burst frequency.

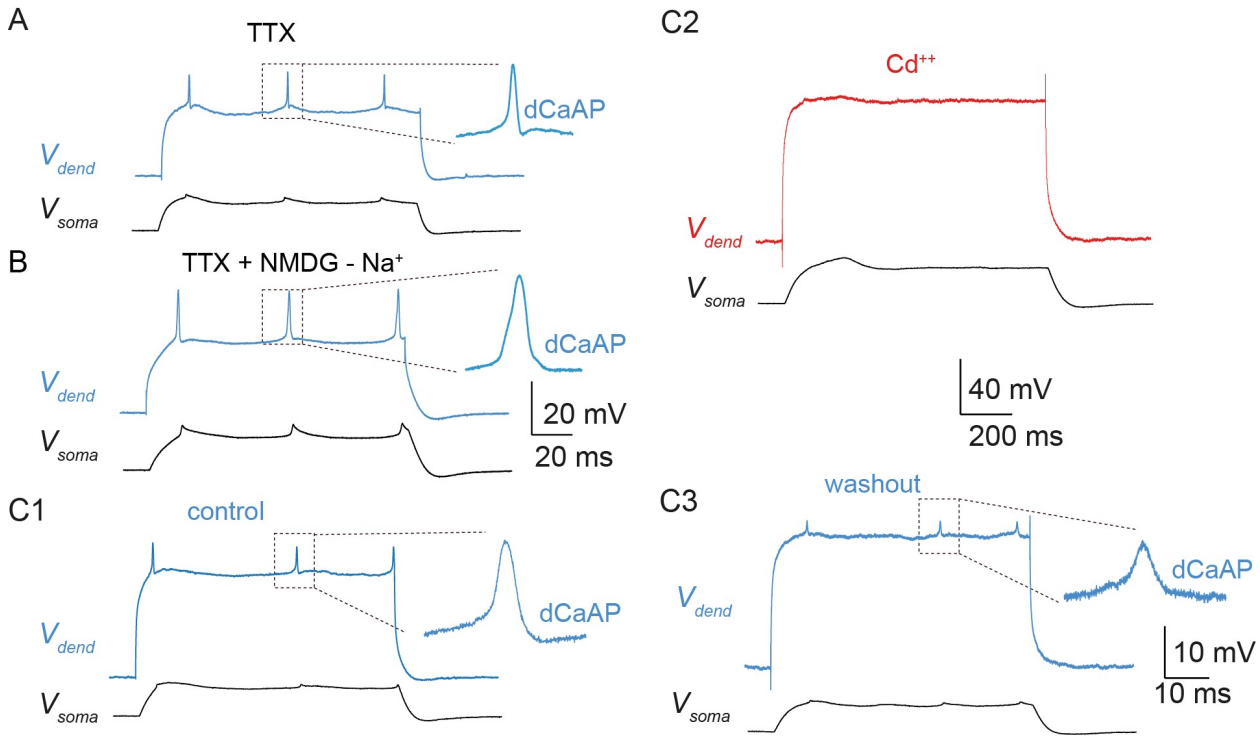

Fig. S3. Dendritic APs were blocked by the voltage gated calcium channel blocker, Cd^{2+}, and were not blocked by Na^{+} channel blocker, TTX.

In all panels dendritic voltage (top trace in blue/red) and somatic voltage (bottom trace in black) are shown in response to a current step injected by the dendritic electrode. **A**. Dendritic APs were recorded in the presence of TTX (1 µM; $n = 4$) in the recording chamber. Dendritic electrode was located 306 µm from the cell body. **B.** As in A in another cell with dendrite electrode 260 µm from the soma. In addition NMDG was used here as substitution for the sodium ions in the extracellular solution to exclude the possibility that dCaAPs are triggered by TTX-insensitive sodium channels. In A and B framed dCaAPs are magnified on the right with scale bar in B. **C.** Step current injected by the dendritic electrode (279 µm from the soma) triggered uncoupled dCaAPs (C1) blocked by Cd^{2+} ($n = 5$ cells) (C2). dCaAPs reappeared after Cd^{2+} washout (C3;

3/5 dendrites recorded for sufficient time, >20 min, to allow washout). The framed dCaAP is magnified on the right. Scale bar for traces in A–C is shown in the bottom of C2.

5

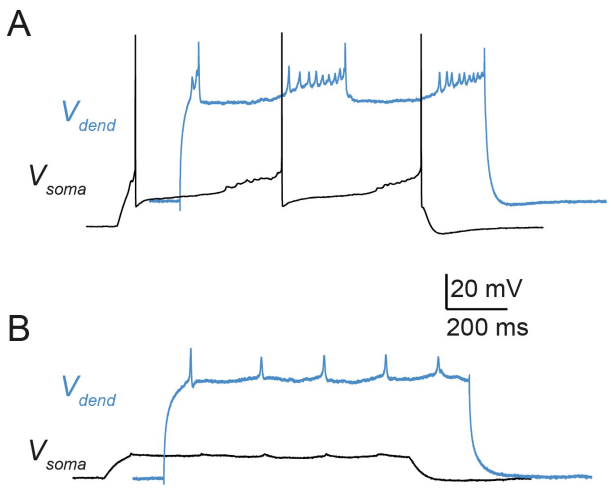

Fig. S4. dCaAPs in the pyramidal neurons of L2/3 in neocortical tissue obtained from tumor patients.

Dendritic voltage (top trace in blue) and somatic voltage (bottom trace in black) in response to current step injected by the dendritic electrode. Dendritic voltage traces are presented with an offset to the right with respect to the somatic traces. **A.** dCaAPs in L2/3 pyramidal neuron in the right temporo-mesial cortex resected from a tumor patient. The neuron was located at depth of 767 μm from the pia and the dendritic electrode was located 291 μm from the soma. The dendrite fired burst of complex-coupled dCaAPs. **B.** Simple-uncoupled dCaAPs recorded in a L2/3 pyramidal neuron (682 μm from the pia with the dendritic electrode at 267 μm from the soma) from the left temporo-mesial cortex resected from a different tumor patient from A.

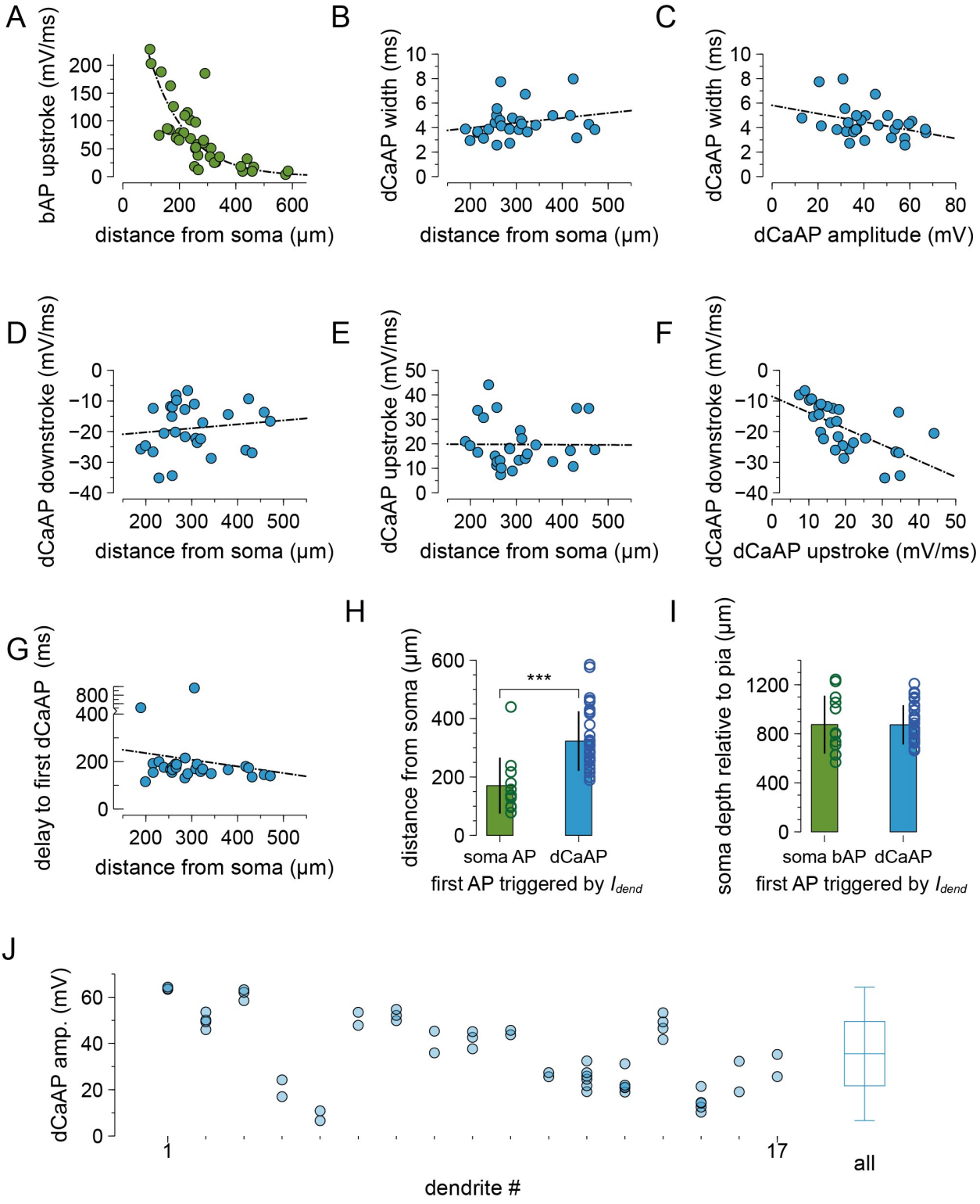
A
bAP upstroke (mV/ms)
distance from soma (µm)
B
dCaAP width (ms)
distance from soma (µm)
C
dCaAP width (ms)
dCaAP amplitude (mV)
D
dCaAP downstroke (mV/ms)
distance from soma (µm)
E
dCaAP upstroke (mV/ms)
distance from soma (µm)
F
dCaAP downstroke (mV/ms)
dCaAP upstroke (mV/ms)
G
delay to first dCaAP (ms)
distance from soma (µm)
H
distance from soma (µm)
***
soma AP
dCaAP
first AP triggered by I_{dend}
I
soma depth relative to pia (µm)
soma bAP
dCaAP
first AP triggered by I_{dend}
J
dCaAP amp. (mV)
1
17
all
dendrite #

Fig. S5. Properties of bAPs and dCaAPs at threshold in human layer 2/3 neurons.

A. bAP upstroke maximal derivative against the distance of the recording electrode from the soma and exponential fit with decay constant λ = 121 µm (n = 31). B. dCaAP upstroke as a function of the recording distance from the soma is weakly correlated with distance (r^2 = 0.1; n = 28). **B–E.** dCaAPs' upstroke (B; $r^2 = 4.6\times10^{-5}$), width (C; at half of the amplitude; r^2 = 0.058), downstroke (D; maximal derivative; r^2 = 0.017) and the delay to the first AP from stimulation onset (E; r^2 = 0.18) are independent or weakly dependent of the distance of the recording electrode from the soma. **F**. dCaAP's widths weakly depended on the dCaAP's amplitudes (r^2 = 0.13). **G**. dCaAP's upstrokes and downstrokes are correlated (r^2 = 0.4). In B–G n = 28 dendrites were used. For consistency with all traces, results are shown for the first dCaAP. **H.** Dendritic electrode evoked somatic APs at proximal regions (170 ± 93 µm from the soma) and dCaAPs at the distal regions (323 ± 99 µm from the soma; Wilcoxon rank-sum test, $p < 10^{-5}$). **I.** Dendritic electrode evoked either somatic APs or dCaAPs independently of the depth of the soma from the pia (the cortical surface). **H**. dCaAP's amplitudes in single near threshold traces in 17 dendrites. Average coefficient of variation was 0.116.

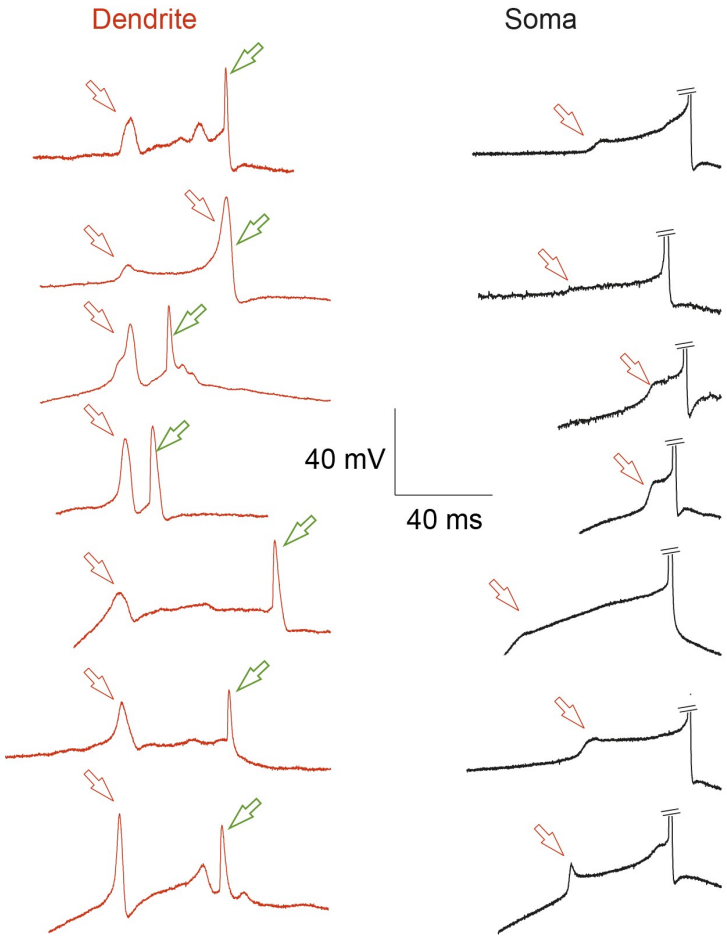

Fig. S6. Gallery of complex dCaAPs.

Left column, dCaAPs (indicated by red arrows) followed by bAPs (green arrows) in response to a dendritic current step injection. *Right column*, Somatic APs (truncated) and dCaAPs (red arrow) recorded at the soma. Somatic APs in these traces were only evoked when preceded by dCaAPs.

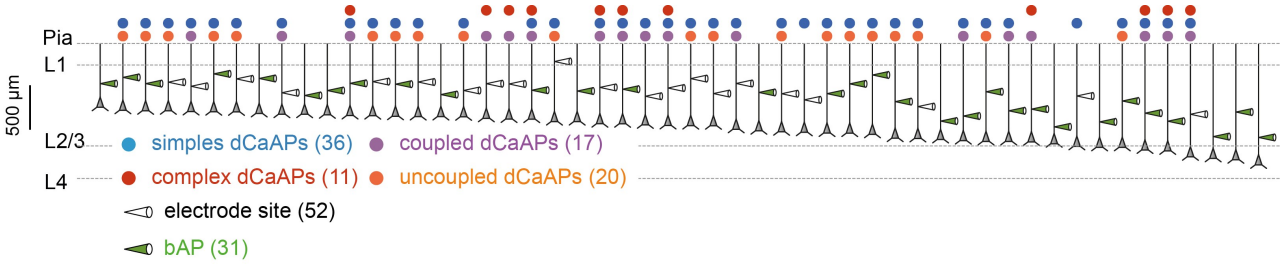

Fig. S7. Summary of bAPs and dCaAPs recordings in L2/3 in the human neocortex.

A schematic drawing summarizing the site of the dendritic electrodes and depth of the somata of the 52 dendrites recoded in this study. Green electrode marker depicts bAP recording. The color-coded dots above each neuron indicate that dCaAPs were either coupled or uncoupled with somatic AP (mutually exclusive classification) and whether dCaAPs were complex and/or simple in these dendrites. The total number of cells for each condition is shown in parentheses.

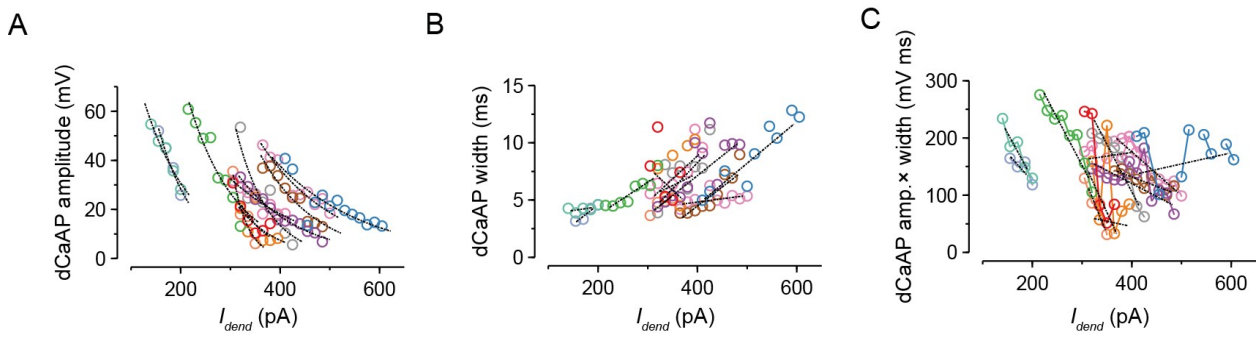

Fig. S8. dCaAPs width and amplitude as a function of the stimulus intensity.

A. (Copied from **Fig. 2E** for comparison) dCaAP amplitudes plotted against the input current strength (I_{dend}) for uncoupled dCaAPs (12 dendrites), fitted by exponential curves (dashed line). Dots in different colors represent dCaAP amplitudes from different cell (12 dendrites). **B.** dCaAP widths at half of the amplitude increases with I_{dend} for the cells in A (a linear fit for each cell is plotted in black dashed line). **C.** dCaAP amplitude × width (an approximation to the dCaAP integral) decreases with I_{dend} namely, the increase in dCaAP width did not counteract the amplitude decay effectively (a linear fit for each cell is plotted in black dashed line).

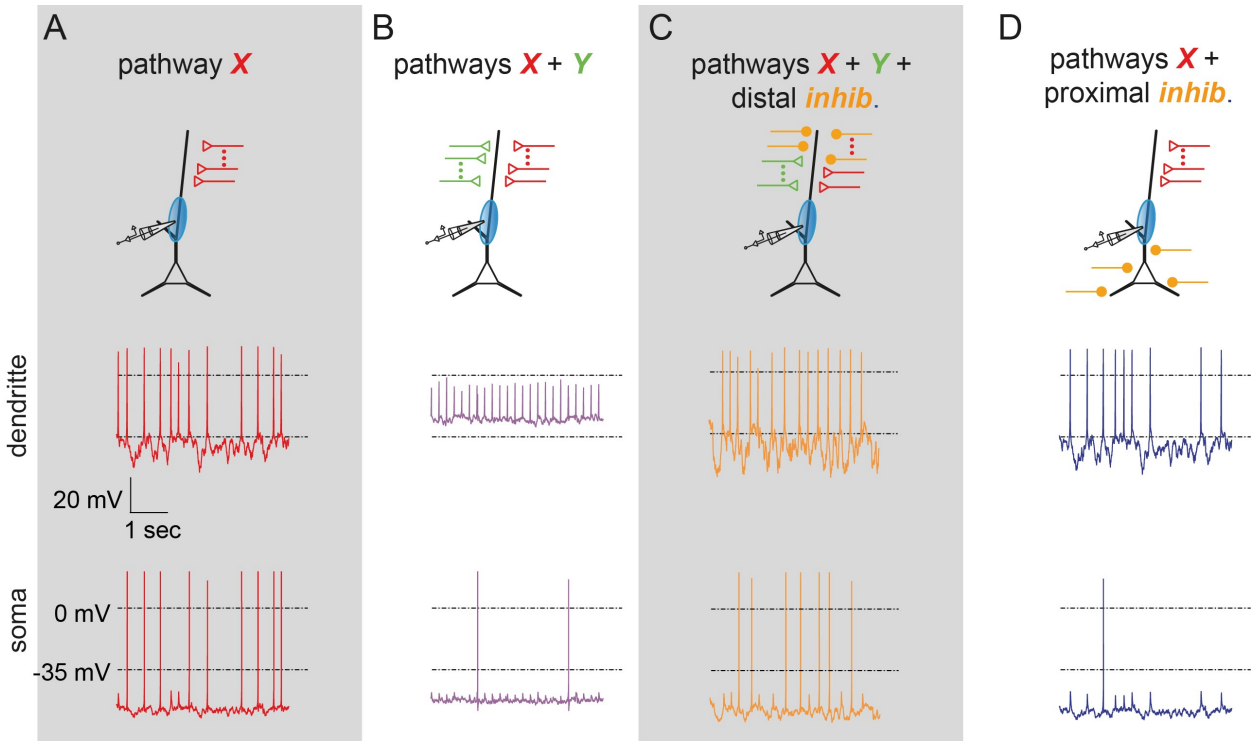

Fig. S9. Combinatorial activation of dCaAPs and somatic APs by the synaptic inputs.
Here we used identical model as in **Fig. 3 (**see also **Methods)** but with dCaAP channels located 287 µm from the soma. Current threshold for dCaAPs (I_{rhe}) was 500 pA. **A.** Pathway *X* with 35 synapses distributed over a subregion of the apical dendrite (as in **Fig 3A**) was able to trigger dCaAPs (top trace) that were coupled with somatic APs (bottom trace). **B.** Pathways *X* + *Y* were less effective in triggering APs at the soma because they suppressed the dCaAP amplitudes. **C**. 35 distal inhibitory synapses [≥ 700 µm from the soma, e.g. inhibition from Martinotti cells (*28*)] in addition to pathways *X* and *Y* caused dCaAPs to regain their amplitudes and impact on the somatic output. **D.** When pathway *X* was activated with 35 proximal inhibitory synapses distributed on the basal dendrite [e.g. inhibition from basket cells (*47*)], dCaAP amplitudes were maximal as in A, but firing of APs at the soma was inhibited. Somatic firing rates were 1.7 Hz

(A), 0.54 Hz (B), 1.5 Hz (C), 0.25 Hz (D). All synapses in the model were active at 20 Hz. Model files can be downloaded from http://modeldb.yale.edu.

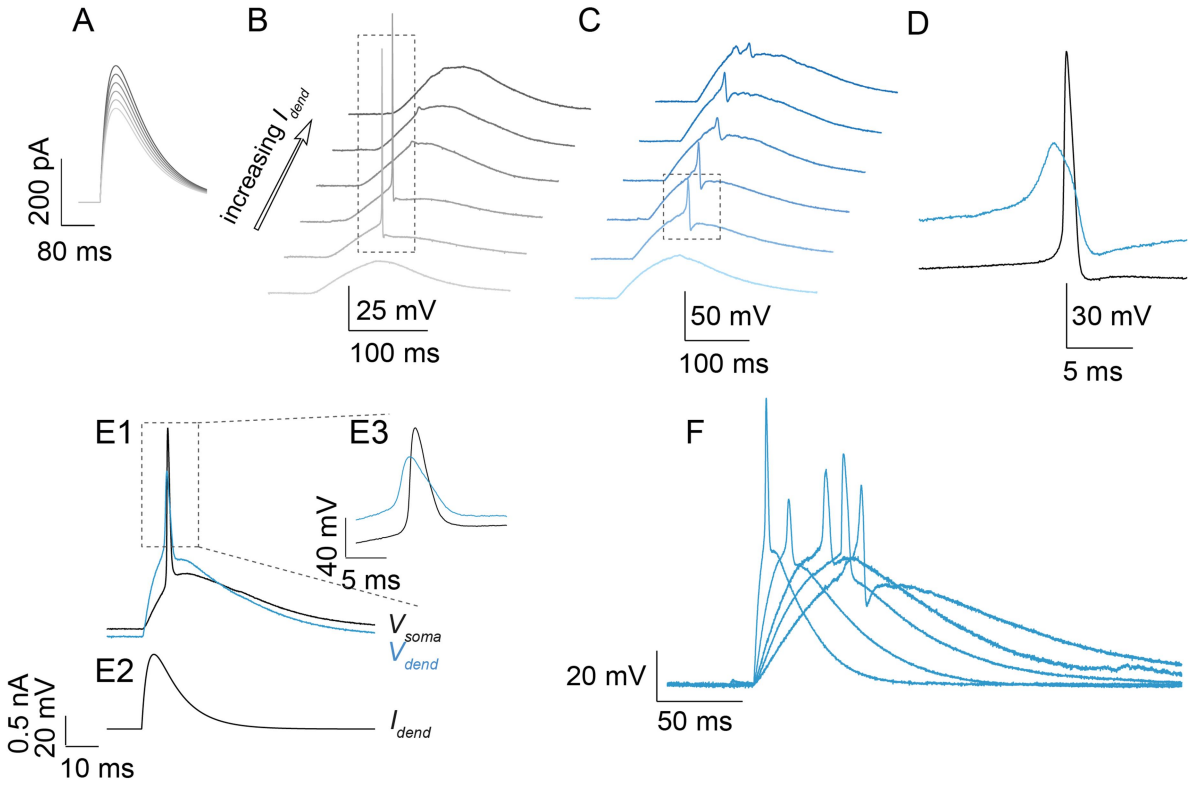

Fig. S10. dCaAP are evoked by transient inputs.

A. I_{dend} injected 260 µm from the cell body, with 20 ms rise time constant and 80 ms decay time constant emulates a transient synaptic barrage to the dendrite. **B-C.** Somatic (B) and dendritic (C) firing as a response for I_{dend} in A. As I_{dend} increased dCaAP amplitude decreased and somatic APs were no longer triggered (top three traces). **D.** Magnified dCaAP (in blue; framed in C) preceded the somatic AP (in black; framed in B). **E.** dCaAP and somatic AP (E1) for I_{dend} with 2 ms rise time constant and 8 ms decay time constant (E2) and magnified dCaAP and somatic AP (E3) for the framed dCaAP in E1. **F.** dCaAPs at threshold in different dendrites for I_{dend} with rise time constant of 2–20 ms and decay time constant of 20–80 ms.

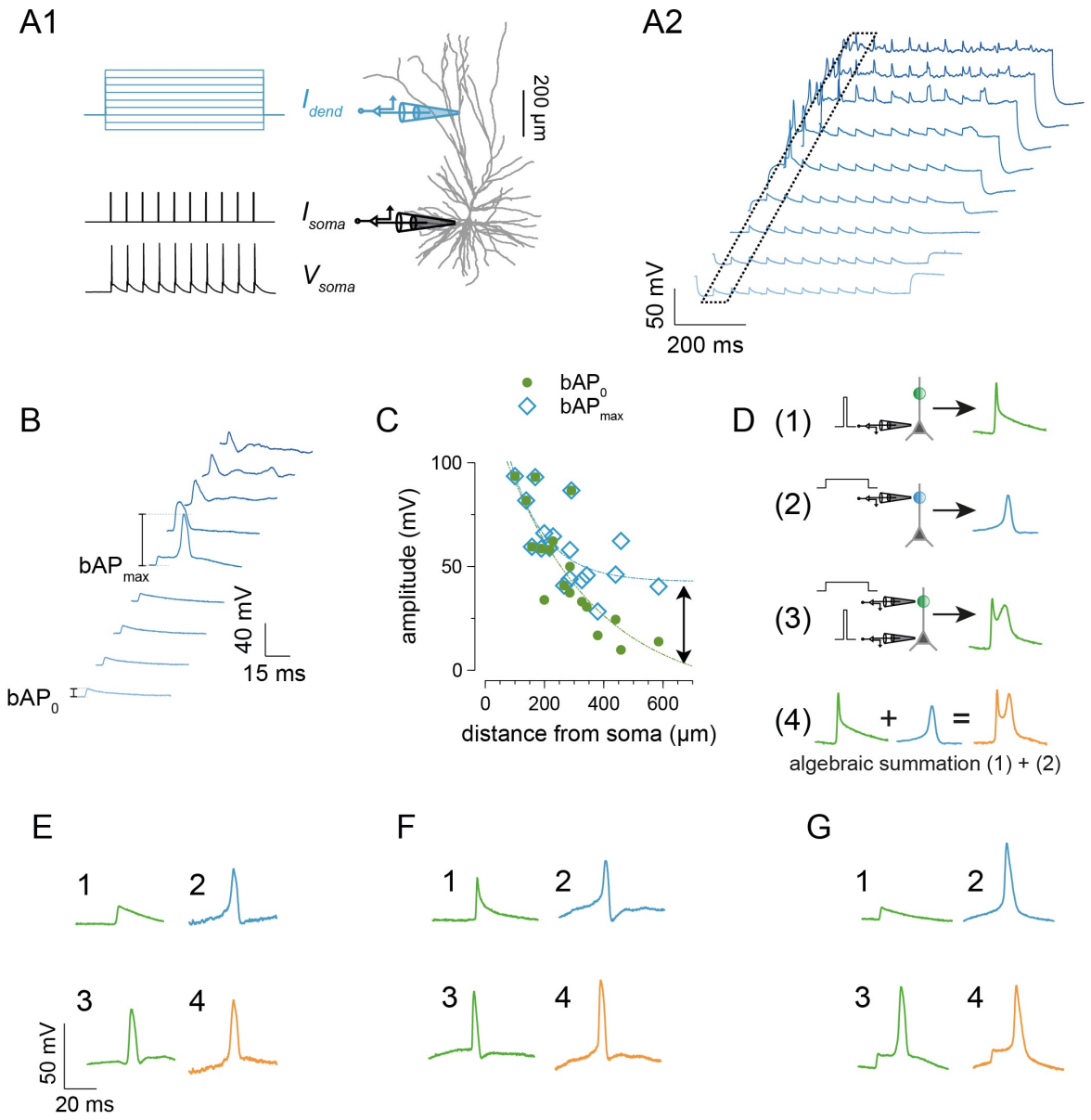

Fig. S11. Non-destructive summation between bAP and dCaAP.

A. Experimental schematic. Stimulus (A1) and recorded voltage traces (A2) for 10 brief pulses (2 ms each) injected to the soma triggering reliable somatic APs. Step currents with increasing strength injected into the dendrite. **B**. Magnified region framed in A2 showing bAPs for each value of I_{dend}. bAP_0 is the amplitude of the bAP at I_{dend} = –100 pA. bAP_{max} is the maximal bAP amplitude (for any I_{dend}). **C.** bAP_0 and bAP_{max} are similar for proximal dendritic sites and diverge

for distal sites (black arrow). **D.** Non-destructive collision of bAPs and dCaAPs: (1) bAP evoked by a brief somatic current stimulus (I_{soma}). (2) dCaAP evoked by I_{dend}. (3) Collision of a bAP and a dCaAP due to I_{soma} + I_{dend}. (4) Algebraic summation of a bAP (from 1) and a dCaAP (from 2) recorded separately. **E–G.** Examples of collisions in other dendrites. Numbers 1–4 corresponds to the conditions in D. The similarity in membrane potential between conditions 3 and 4 suggests that the summation of bAPs and dCaAPs is not destructive.

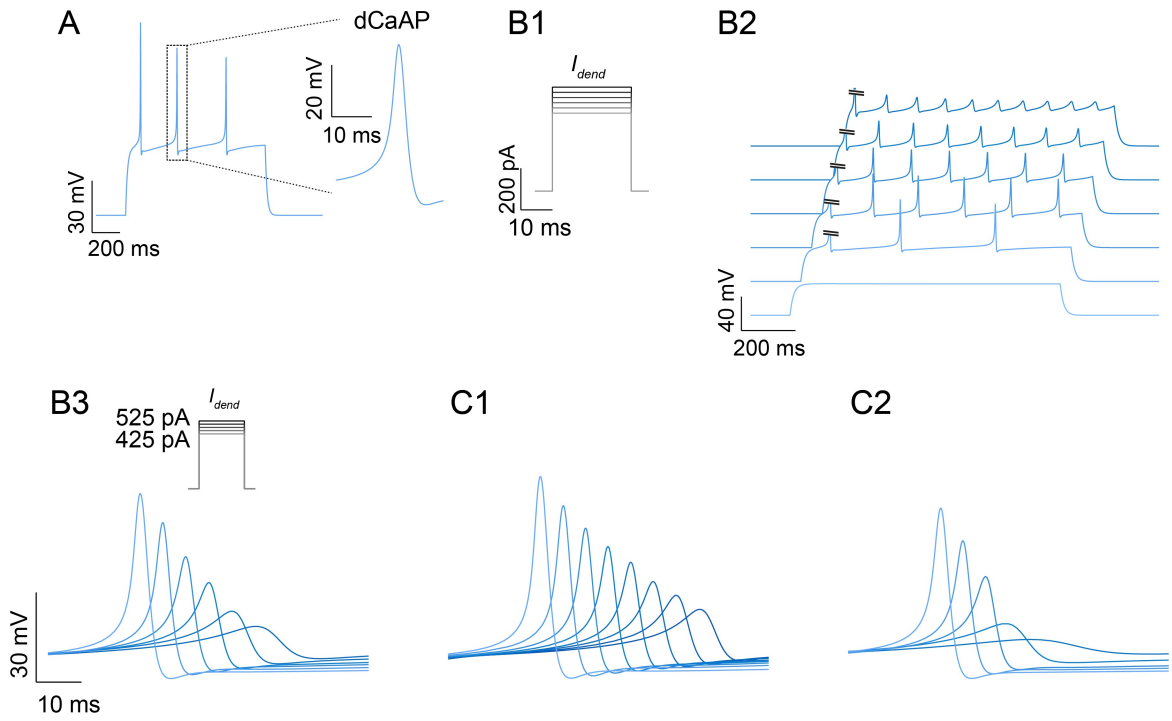

Fig. S12. Modeling dCaAPs with known calcium and potassium channels.

We modeled an isopotential segment of a dendrite in NEURON simulation environment with high voltage Ca^{2+} (HVA-like) channels (*48*), voltage and Ca^{2+} dependent potassium (BK-like) channels (*49*) and leak channels such that R_{in} = 92 MΩ and τ_m = 14 ms. In addition to the functional relevance, BK channels are diverse and know to express in human neurons (*50*). For the intracellular Ca^{2+} ions clearance we used a Ca^{2+} pump from (*51*). Only the time constants of the BK-like channels gates were modified to achieve the characteristic waveform of the dCaAP (**Table S2**; model files can be downloaded from http://modeldb.yale.edu). **A.** Our model faithfully reproduced dCaAPs' amplitude, width and the slow rise time we observed *in vitro*. **B.** As a function of the input (B1) dCaAP amplitude decayed (B2, B3) similar to the results shown in **Fig. 2D**. We could not reproduce this behavior without the Ca^{2+} and voltage dependence of the BK-like channels. For the sake of simplicity we did not use additional mechanism to reduce the

high amplitude of the first dCaAP in each trace as observed *in vitro* (truncated dCaAPs). **C1.** The dCaAPs' decay was weaker than in B3 (as a function of I_{dend}) for faster Ca^{2+} pump time constant (40 ms). **C2** The dCaAPs' decay was stronger than in B3 for slower Ca^{2+} pump time constant. (80 ms ; **Table S2**).

Table S1: Summary of patients' details and diagnosis.

#	Age	Age at epilepsy onset	Sex	Diagnosis	Recent antiepileptic drugs (mg/day)
1	26	19	F	TLE	LTG (500), ZNS (500)
2	29	20	F	TLE	LAC (400), LEV (3000)
3	35	27	M	TLE	LEV (3000), LTG (400)
4	41	25	F	TLE	LTG (400), ZNS (300)
5	32	27	F	TLE	OXC (1500), LEV (3000)
6	54	16	F	TLE	OXC (1200), LTG (200)
7	20	16	F	TLE	LTG (600)
8	42	5	F	TLE	TPM (300), BRV (300)
9	28	13	M	TLE	VPA (2000), OXC (2100)
10	22	12	F	TLE	OXC (1200)
11	18	12	M	TLE	OXC (2400)
12	45	16	M	TLE	ZNS (200), OXC (1200), CLB (10)
13	32	27	M	TLE	LAC (400), LEV (3000), LTG (150)
14	15	–	M	TLE	LEV (2000)
15	26	11	M	MLE	OXC (2100), CLB (20)
16	43	29	M	TLE	LTG (500), LAC (500), CLB (20)
17	36	12	M	TLE	LTG (200), LAC (400)
18	26	14	M	TLE	OXC (1800), TPM (75)
19	31	21	M	TLE	LAC (600), BRV (200)
20	39	1	F	TLE	LTG (300)
21	22	15	M	TLE	LTG (800), ESL (1200)
22	40	26	M	TLE	CBZ (1200), TPM (250), BRV (200)
23	27	10	M	TLE	LAC (400), BRV (50)
24	30	23	M	TLE	LEV (3000),LAC (300),CLB (20)
25	21	14	F	TLE	LTG (900)
26	34	6	M	TLE	LTG (700)
27	21	17	F	TLE	OXC (1000)
28	68	–	M	glioblastoma[1]	
29	63	–	F	glioblastoma[2]	
30	37	–	F	dysembyroplastic neuroepithelial tumor[3]	

M: Male; F: Female; TLE: temporal lobe epilepsy; MLE: multilobar epilepsy;

Antiepileptic drugs specified: BRV: brivaracetam; CBZ: carbamazepine; CLB: clobazam; ESL: eslicarbazepine acetate; LAC: lacosamide; LEV: levetiracetam; LTG: lamotrigine; OXC: oxcarbazepine; TPM: topiramate; VPA: valproate; ZNS: zonisamide;

1. Left frontal region
2. Right temporomesial region and insula
3. Left temporomesial region

Table S2: Summary of main biophysical parameters for the model in Fig. S12.

Channel	Parameter	Value	Modified parameters
BK-like	source	Khaliq et al., (2003)	
	$g_{max}(S/cm^2)$	0.03	
	$\tau_m(ms)$	$\left[0.505 + \frac{1000}{(exp((v+86.4)/10.1) + exp(-(v-33.3)/10))}\right] \times Fm_\tau$	$Fm_\tau = 5$
	$\tau_h(ms)$	$\left[1.9 + \frac{1000}{(exp((v+48.5)/5.2) + exp(-(v-54.2)/12.9))}\right] \times Fh_\tau$	$Fh_\tau = 50$
	$\tau_z(ms)$	1	
HVA-like	source	Reuveni et al., (1993)	
	$g_{max}(S/cm^2)$	0.0005	
Ca^{2+} pump	source	Destexhe et al. (1993)	
		$\frac{d[Ca]_i}{dt} = -KI_{Ca} - ([Ca]_i - [Ca]_b)/\tau_{Ca}$	$\tau_{Ca} = \begin{cases} 40 \text{ ms, Fig. S12C1} \\ 60 \text{ ms, Fig. S12B3} \\ 80 \text{ ms, Fig. S12C2} \end{cases}$

References and Notes

1. J. DeFelipe, L. Alonso-Nanclares, J. I. Arellano, Microstructure of the neocortex: Comparative aspects. *J. Neurocytol.* **31**, 299–316 (2002). doi:10.1023/A:1024130211265 Medline

2. H. Mohan, M. B. Verhoog, K. K. Doreswamy, G. Eyal, R. Aardse, B. N. Lodder, N. A. Goriounova, B. Asamoah, A. B. C. B. Brakspear, C. Groot, S. van der Sluis, G. Testa-Silva, J. Obermayer, Z. S. R. M. Boudewijns, R. T. Narayanan, J. C. Baayen, I. Segev, H. D. Mansvelder, C. P. J. de Kock, Dendritic and Axonal Architecture of Individual Pyramidal Neurons across Layers of Adult Human Neocortex. *Cereb. Cortex* **25**, 4839–4853 (2015). doi:10.1093/cercor/bhv188 Medline

3. Y. Deitcher, G. Eyal, L. Kanari, M. B. Verhoog, G. A. Atenekeng Kahou, H. D. Mansvelder, C. P. J. de Kock, I. Segev, Comprehensive Morpho-Electrotonic Analysis Shows 2 Distinct Classes of L2 and L3 Pyramidal Neurons in Human Temporal Cortex. *Cereb. Cortex* **27**, 5398–5414 (2017). doi:10.1093/cercor/bhx226 Medline

4. J. Waters, M. Larkum, B. Sakmann, F. Helmchen, Supralinear Ca2+ influx into dendritic tufts of layer 2/3 neocortical pyramidal neurons in vitro and in vivo. *J. Neurosci.* **23**, 8558–8567 (2003). doi:10.1523/JNEUROSCI.23-24-08558.2003 Medline

5. M. E. Larkum, J. Waters, B. Sakmann, F. Helmchen, Dendritic spikes in apical dendrites of neocortical layer 2/3 pyramidal neurons. *J. Neurosci.* **27**, 8999–9008 (2007). doi:10.1523/JNEUROSCI.1717-07.2007 Medline

6. L. Beaulieu-Laroche, E. H. S. Toloza, M.-S. van der Goes, M. Lafourcade, D. Barnagian, Z. M. Williams, E. N. Eskandar, M. P. Frosch, S. S. Cash, M. T. Harnett, Enhanced Dendritic Compartmentalization in Human Cortical Neurons. *Cell* **175**, 643–651.e14 (2018). doi:10.1016/j.cell.2018.08.045 Medline

7. S. L. Smith, I. T. Smith, T. Branco, M. Häusser, Dendritic spikes enhance stimulus selectivity in cortical neurons in vivo. *Nature* **503**, 115–120 (2013). doi:10.1038/nature12600 Medline

8. J. J. Moore, P. M. Ravassard, D. Ho, L. Acharya, A. L. Kees, C. Vuong, M. R. Mehta, Dynamics of cortical dendritic membrane potential and spikes in freely behaving rats. *Science* **355**, eaaj1497 (2017). doi:10.1126/science.aaj1497 Medline

9. B. Sivyer, S. R. Williams, Direction selectivity is computed by active dendritic integration in retinal ganglion cells. *Nat. Neurosci.* **16**, 1848–1856 (2013). doi:10.1038/nn.3565 Medline

10. S. Crochet, P. Fuentealba, I. Timofeev, M. Steriade, Selective amplification of neocortical neuronal output by fast prepotentials in vivo. *Cereb. Cortex* **14**, 1110–1121 (2004). doi:10.1093/cercor/bhh071 Medline

11. Y. Kim, C.-L. Hsu, M. S. Cembrowski, B. D. Mensh, N. Spruston, Dendritic sodium spikes are required for long-term potentiation at distal synapses on hippocampal pyramidal neurons. *eLife* **4**, e06414 (2015). doi:10.7554/eLife.06414 Medline

12. M. E. Larkum, J. J. Zhu, B. Sakmann, Dendritic mechanisms underlying the coupling of the dendritic with the axonal action potential initiation zone of adult rat layer 5 pyramidal

neurons. *J. Physiol.* **533**, 447–466 (2001). doi:10.1111/j.1469-7793.2001.0447a.x Medline

13. N. L. Golding, N. Spruston, Dendritic sodium spikes are variable triggers of axonal action potentials in hippocampal CA1 pyramidal neurons. *Neuron* **21**, 1189–1200 (1998). doi:10.1016/S0896-6273(00)80635-2 Medline

14. L. M. Palmer, A. S. Shai, J. E. Reeve, H. L. Anderson, O. Paulsen, M. E. Larkum, NMDA spikes enhance action potential generation during sensory input. *Nat. Neurosci.* **17**, 383–390 (2014). doi:10.1038/nn.3646 Medline

15. M. E. Larkum, J. J. Zhu, B. Sakmann, A new cellular mechanism for coupling inputs arriving at different cortical layers. *Nature* **398**, 338–341 (1999). doi:10.1038/18686 Medline

16. N. L. Golding, H. Y. Jung, T. Mickus, N. Spruston, Dendritic calcium spike initiation and repolarization are controlled by distinct potassium channel subtypes in CA1 pyramidal neurons. *J. Neurosci.* **19**, 8789–8798 (1999). doi:10.1523/JNEUROSCI.19-20-08789.1999 Medline

17. C. Labarrera, Y. Deitcher, A. Dudai, B. Weiner, A. Kaduri Amichai, N. Zylbermann, M. London, Adrenergic Modulation Regulates the Dendritic Excitability of Layer 5 Pyramidal Neurons In Vivo. *Cell Rep.* **23**, 1034–1044 (2018). doi:10.1016/j.celrep.2018.03.103 Medline

18. J. Schiller, G. Major, H. J. Koester, Y. Schiller, NMDA spikes in basal dendrites of cortical pyramidal neurons. *Nature* **404**, 285–289 (2000). doi:10.1038/35005094 Medline

19. M. E. Larkum, K. M. M. Kaiser, B. Sakmann, Calcium electrogenesis in distal apical dendrites of layer 5 pyramidal cells at a critical frequency of back-propagating action potentials. *Proc. Natl. Acad. Sci. U.S.A.* **96**, 14600–14604 (1999). doi:10.1073/pnas.96.25.14600 Medline

20. M. E. Larkum, T. Nevian, M. Sandler, A. Polsky, J. Schiller, Synaptic integration in tuft dendrites of layer 5 pyramidal neurons: A new unifying principle. *Science* **325**, 756–760 (2009). doi:10.1126/science.1171958 Medline

21. J. J. Zhu, Maturation of layer 5 neocortical pyramidal neurons: Amplifying salient layer 1 and layer 4 inputs by Ca2+ action potentials in adult rat tuft dendrites. *J. Physiol.* **526**, 571–587 (2000). doi:10.1111/j.1469-7793.2000.00571.x Medline

22. J. Schiller, Y. Schiller, G. Stuart, B. Sakmann, Calcium action potentials restricted to distal apical dendrites of rat neocortical pyramidal neurons. *J. Physiol.* **505**, 605–616 (1997). doi:10.1111/j.1469-7793.1997.605ba.x Medline

23. M. L. Hines, N. T. Carnevale, The NEURON simulation environment. *Neural Comput.* **9**, 1179–1209 (1997). doi:10.1162/neco.1997.9.6.1179 Medline

24. M. London, M. Häusser, Dendritic computation. *Annu. Rev. Neurosci.* **28**, 503–532 (2005). doi:10.1146/annurev.neuro.28.061604.135703 Medline

25. A. Polsky, B. W. Mel, J. Schiller, Computational subunits in thin dendrites of pyramidal cells. *Nat. Neurosci.* **7**, 621–627 (2004). doi:10.1038/nn1253 Medline

26. A. Losonczy, J. C. Magee, Integrative properties of radial oblique dendrites in hippocampal CA1 pyramidal neurons. *Neuron* **50**, 291–307 (2006). doi:10.1016/j.neuron.2006.03.016 Medline

27. E. Boldog, T. E. Bakken, R. D. Hodge, M. Novotny, B. D. Aevermann, J. Baka, S. Bordé, J. L. Close, F. Diez-Fuertes, S.-L. Ding, N. Faragó, Á. K. Kocsis, B. Kovács, Z. Maltzer, J. M. McCorrison, J. A. Miller, G. Molnár, G. Oláh, A. Ozsvár, M. Rózsa, S. I. Shehata, K. A. Smith, S. M. Sunkin, D. N. Tran, P. Venepally, A. Wall, L. G. Puskás, P. Barzó, F. J. Steemers, N. J. Schork, R. H. Scheuermann, R. S. Lasken, E. S. Lein, G. Tamás, Transcriptomic and morphophysiological evidence for a specialized human cortical GABAergic cell type. *Nat. Neurosci.* **21**, 1185–1195 (2018). doi:10.1038/s41593-018-0205-2 Medline

28. A. Gidon, I. Segev, Principles governing the operation of synaptic inhibition in dendrites. *Neuron* **75**, 330–341 (2012). doi:10.1016/j.neuron.2012.05.015 Medline

29. A. T. Gulledge, G. J. Stuart, Excitatory actions of GABA in the cortex. *Neuron* **37**, 299–309 (2003). doi:10.1016/S0896-6273(02)01146-7 Medline

30. G. M. Shepherd, R. K. Brayton, Logic operations are properties of computer-simulated interactions between excitable dendritic spines. *Neuroscience* **21**, 151–165 (1987). doi:10.1016/0306-4522(87)90329-0 Medline

31. M. Minsky, S. A. Papert, *Perceptrons: An Introduction to Computational Geometry* (MIT Press, 1969).

32. F. Rosenblatt, *The Perceptron, a Perceiving and Recognizing Automaton: (Project Para)* (Cornell Aeronautical Laboratory, 1957).

33. G. Eyal, M. B. Verhoog, G. Testa-Silva, Y. Deitcher, R. Benavides-Piccione, J. DeFelipe, C. P. J. de Kock, H. D. Mansvelder, I. Segev, Human Cortical Pyramidal Neurons: From Spines to Spikes via Models. *Front. Cell. Neurosci.* **12**, 181 (2018). doi:10.3389/fncel.2018.00181 Medline

34. P. Poirazi, T. Brannon, B. W. Mel, Pyramidal neuron as two-layer neural network. *Neuron* **37**, 989–999 (2003). doi:10.1016/S0896-6273(03)00149-1 Medline

35. G. Testa-Silva, S. Honnuraiah, C. French, J. King, K. Drummond, L. M. Palmer, G. J. Stuart, "NMDA spikes in human neocortex," program no. 463.12, *2018 Neuroscience Meeting Planner*, Society for Neuroscience, San Diego, CA, 3 to 7 November 2018.

36. A. Gidon, T. A. Zolnik, P. Fidzinski, F. Bolduan, A. Papoutsi, P. Poirazi, M. Holtkamp, I. Vida, M. E. Larkum, Dendritic action potentials and computation in human layer 2/3 cortical neurons. Zenodo (2020); https://doi.org/10.5281/zenodo.3530043.

37. G. Testa-Silva, M. B. Verhoog, N. A. Goriounova, A. Loebel, J. Hjorth, J. C. Baayen, C. P. J. de Kock, H. D. Mansvelder, Human synapses show a wide temporal window for spike-timing-dependent plasticity. *Front. Synaptic Neurosci.* **2**, 12 (2010). doi:10.3389/fnsyn.2010.00012 Medline

38. J. T. Ting, T. L. Daigle, Q. Chen, G. Feng, Acute brain slice methods for adult and aging animals: Application of targeted patch clamp analysis and optogenetics. *Methods Mol. Biol.* **1183**, 221–242 (2014). doi:10.1007/978-1-4939-1096-0_14 Medline

39. T. Nevian, M. E. Larkum, A. Polsky, J. Schiller, Properties of basal dendrites of layer 5 pyramidal neurons: A direct patch-clamp recording study. *Nat. Neurosci.* **10**, 206–214 (2007). doi:10.1038/nn1826 Medline

40. S. A. Booker, J. Song, I. Vida, Whole-cell patch-clamp recordings from morphologically- and neurochemically-identified hippocampal interneurons. *J. Vis. Exp.* **91**, e51706 (2014). doi:10.3791/51706 Medline

41. S. Preibisch, S. Saalfeld, P. Tomancak, Globally optimal stitching of tiled 3D microscopic image acquisitions. *Bioinformatics* **25**, 1463–1465 (2009). doi:10.1093/bioinformatics/btp184

42. L. Feng, T. Zhao, J. Kim, neuTube 1.0: A New Design for Efficient Neuron Reconstruction Software Based on the SWC Format. *eNeuro* **2**, ENEURO.0049-14.2014 (2015). doi:10.1523/ENEURO.0049-14.2014 Medline

43. G. Eyal, M. B. Verhoog, G. Testa-Silva, Y. Deitcher, J. C. Lodder, R. Benavides-Piccione, J. Morales, J. DeFelipe, C. P. de Kock, H. D. Mansvelder, I. Segev, Unique membrane properties and enhanced signal processing in human neocortical neurons. *eLife* **5**, e16553 (2016). doi:10.7554/eLife.16553 Medline

44. R. D. Traub, R. K. Wong, R. Miles, H. Michelson, A model of a CA3 hippocampal pyramidal neuron incorporating voltage-clamp data on intrinsic conductances. *J. Neurophysiol.* **66**, 635–650 (1991). doi:10.1152/jn.1991.66.2.635 Medline

45. L. Sarid, R. Bruno, B. Sakmann, I. Segev, D. Feldmeyer, Modeling a layer 4-to-layer 2/3 module of a single column in rat neocortex: Interweaving in vitro and in vivo experimental observations. *Proc. Natl. Acad. Sci. U.S.A.* **104**, 16353–16358 (2007). doi:10.1073/pnas.0707853104 Medline

46. P. Rhodes, The properties and implications of NMDA spikes in neocortical pyramidal cells. *J. Neurosci.* **26**, 6704–6715 (2006). doi:10.1523/JNEUROSCI.3791-05.2006 Medline

47. A. Gupta, Y. Wang, H. Markram, Organizing principles for a diversity of GABAergic interneurons and synapses in the neocortex. *Science* **287**, 273–278 (2000). doi:10.1126/science.287.5451.273 Medline

48. I. Reuveni, A. Friedman, Y. Amitai, M. J. Gutnick, Stepwise repolarization from Ca2+ plateaus in neocortical pyramidal cells: Evidence for nonhomogeneous distribution of HVA Ca2+ channels in dendrites. *J. Neurosci.* **13**, 4609–4621 (1993). doi:10.1523/JNEUROSCI.13-11-04609.1993 Medline

49. Z. M. Khaliq, N. W. Gouwens, I. M. Raman, The contribution of resurgent sodium current to high-frequency firing in Purkinje neurons: An experimental and modeling study. *J. Neurosci.* **23**, 4899–4912 (2003). doi:10.1523/JNEUROSCI.23-12-04899.2003 Medline

50. R. Latorre, K. Castillo, W. Carrasquel-Ursulaez, R. V. Sepulveda, F. Gonzalez-Nilo, C. Gonzalez, O. Alvarez, Molecular Determinants of BK Channel Functional Diversity and Functioning. *Physiol. Rev.* **97**, 39–87 (2017). doi:10.1152/physrev.00001.2016 Medline

51. A. Destexhe, A. Babloyantz, T. J. Sejnowski, Ionic mechanisms for intrinsic slow oscillations in thalamic relay neurons. *Biophys. J.* **65**, 1538–1552 (1993). doi:10.1016/S0006-3495(93)81190-1 Medline